Large-eddy simulation of decaying isotropic turbulence using the flowfield dependent variation method

Seyi F. Olatoyinbo, Sarma L. Rani and Abdelkader Frendi
Department of Mechanical and Aerospace Engineering, University of Alabama in Huntsville, Huntsville, Alabama, USA

Received 24 July 2015
Revised 23 October 2015
Accepted 27 October 2015

Abstract

Purpose – The purpose of this study is to investigate the accuracy and applicability of the Flowfield Dependent Variation (FDV) method for large-eddy simulations (LES) of decaying isotropic turbulence.

Design/methodology/approach – In an earlier paper, the FDV method was successfully demonstrated for simulations of laminar flows with speeds varying from low subsonic to high supersonic Mach numbers. In the current study, the FDV method, implemented in a finite element framework, is used to perform LESs of decaying isotropic turbulence. The FDV method is fundamentally derived from the Lax–Wendroff Scheme (LWS) by replacing the explicit time derivatives in LWS with a weighted combination of explicit and implicit time derivatives. The increased implicitness and the inherent numerical dissipation of FDV contribute to the scheme's numerical stability and monotonicity. Understanding the role of numerical dissipation that is inherent to the FDV method is essential for the maturation of FDV into a robust scheme for LES of turbulent flows. Accordingly, three types of LES of decaying isotropic turbulence were performed. The first two types of LES utilized explicit subgrid scale (SGS) models, namely, the constant-coefficient Smagorinsky and dynamic Smagorinsky models. In the third, no explicit SGS model was employed; instead, the numerical dissipation inherent to FDV was used to emulate the role played by explicit SGS models. Such an approach is commonly known as Implicit LES (ILES). A new formulation was also developed for quantifying the FDV numerical viscosity that principally arises from the convective terms of the filtered Navier–Stokes equations.

Findings – The temporal variation of the turbulent kinetic energy and enstrophy and the energy spectra are presented and analyzed. At all grid resolutions, the temporal profiles of kinetic energy showed good agreement with $t^{(-1.43)}$ theoretical scaling in the fully developed turbulent flow regime, where t represents time. The energy spectra also showed reasonable agreement with the Kolmogorov's $k^{(-5/3)}$ power law in the inertial subrange, with the spectra moving closer to the Kolmogorov scaling at higher-grid resolutions. The intrinsic numerical viscosity and the dissipation rate of the FDV scheme are quantified, both in physical and spectral spaces, and compared with those of the two SGS LES runs. Furthermore, at a finite number of flow realizations, the numerical viscosities of FDV and of the Streamline Upwind/Petrov–Galerkin (SUPG) finite element method are compared. In the initial stages of turbulence development, all three LES cases have similar viscosities. But, once the turbulence is fully developed, implicit LES is less dissipative compared to the two SGS LES runs. It was also observed that the SUPG method is significantly more dissipative than the three LES approaches.

Research limitations/implications – Just as any computational method, the limitations are based on the available computational resources.

This work was made possible, in part, by a grant of high performance computing resources and technical support from the Alabama Supercomputer Authority. Support for the first author was provided in part by the National Space Research & Development Agency (NASRDA), Nigeria, and the Mechanical and Aerospace Engineering Department at the University of Alabama in Huntsville through a graduate teaching assistantship.

International Journal of Numerical Methods for Heat & Fluid Flow
Vol. 27 No. 1, 2017
pp. 235-262

0961-5539
DOI 10.1108/HFF-07-2015-0290

Practical implications – Solving problems involving turbulent flows is by far the biggest challenge facing engineers and scientists in the twenty-first century, this is the road that the authors have embarked upon in this paper and the road ahead of is very long.

Social implications – Understanding turbulence is a very lofty goal and a challenging one as well; however, if the authors succeed, the rewards are limitless.

Originality/value – The derivation of an explicit expression for the numerical viscosity tensor of FDV is an important contribution of this study, and is a crucial step forward in elucidating the fundamental properties of the FDV method. The comparison of viscosities for the three LES cases and the SUPG method has important implications for the application of ILES approach for turbulent flow simulations.

Keywords Finite element method, Flowfield Dependent Variation method, Implicit LES, Isotropic turbulence, Large-eddy simulation, Numerical dissipation rate, Numerical viscosity

Paper type Research paper

1. Introduction

Large-eddy simulation (LES) has emerged as a popular modeling approach for turbulent flows. This trend has been driven by the need to balance two competing requirements: the finer resolution of flow physics and the moderation of computational cost. The cost savings in LES are achieved through the use of scale separation, i.e. turbulent scales in the energy-containing region and part of the inertial subrange of the energy spectrum are resolved, while the dynamics of smaller unresolved scales are modeled using subgrid scale (SGS) models.

Large-eddy simulation is a compromise between direct numerical simulation (DNS), which involves resolving all turbulent scales, and Reynolds Averaged Navier–Stokes Simulation (RANS), which consists of modeling the effects of all scales. Thus, LES is superior to RANS in providing insights into the larger scales of the underlying turbulence. It is also computationally less expensive than DNS, with the added advantage of overcoming the Reynolds number restriction on DNS. Therefore, LES is considered to be a suitable approach for three-dimensional (3-D) unsteady simulations of turbulent flows of engineering relevance (Garnier *et al.*, 2009). The governing equations for LES consist of 3-D filtered Navier–Stokes equations. The filtered equations contain unclosed terms representing the effects of unresolved subgrid-scale eddies, which are typically closed through explicit SGS models. An alternative approach involves the use of dissipation inherent to the numerical scheme to emulate the role of SGS models, commonly referred to as implicit LES (ILES).

In general, large-eddy simulations are carried out using finite difference or finite volume methods. Recently, LES in conjunction with the finite element method (FEM) has received some attention. The use of FEM for LES was pioneered by Jansen (1995) who studied flow over a NACA 4412 airfoil. Jansen (1999) presented two FEM-based approaches, namely, Galerkin/Least-Squares (GLS) and Streamline Upwind/Petrov–Galerkin (SUPG) methods. Chalot *et al.* (1998) studied the use of GLS/FEM to perform LES of compressible flows, and found that the least-squares operator inherent to GLS method is incapable of acting as a proper SGS model for decaying "inviscid" isotropic turbulence. Tejada-Martínez and Jansen (2004) used the SUPG/FEM formulation to simulate incompressible decaying isotropic turbulence with a dynamic Smagorinsky SGS model. Their work showed that the filter width ratio had a significant influence on LES predictions, while the type of test filter did not strongly impact the results. Levasseur *et al.* (2006) used GLS/FEM formulation for simulating compressible decaying isotropic turbulence at infinite Reynolds numbers using the standard Smagorinsky, dynamic Smagorinsky and variational multiscale (VMS) SGS models. They showed that the least-squares stabilization is unsuitable for ILES calculations, and that the VMS model performs comparably to dynamic Smagorinsky model.

The Flowfield Dependent Variation (FDV) method was developed by Chung *et al.* (Yoon and Chung, 1996; Yoon *et al.*, 1998) to simulate flows characterized by a wide range of spatial and temporal scales, and multiple speeds. The FDV method was built with the idea of being a unified numerical scheme for solving complex, multiphysics problems. Thus, it is possible to recover most of the current finite difference-, finite volume- and finite element-based schemes from the FDV method as special cases (Chung, 2002). Prior applications of the FDV method include: simulations of heat transfer and fluid dynamics problems (Moon *et al.*, 2001), computation of non-ideal relativistic astrophysics and hydrodynamic flows (Richardson and Chung, 2002; Richardson *et al.*, 2010), prediction of ignition over-pressure in launch vehicle acoustics (Canabal and Frendi, 2006) and recently, the numerical simulations of low- to high-Mach number laminar flows (Girgis *et al.*, 2015).

In the current study, we investigate the applicability of the FDV scheme, implemented in a Taylor–Galerkin-based FEM framework, to LESs of decaying isotropic turbulence. The principal objectives of this study are to:

- develop a new formulation for the numerical viscosity inherent to the FDV scheme;
- quantify this viscosity both in physical and spectral spaces;
- establish that FDV's numerical viscosity coupled with the method's increased implicitness (compared to Lax–Wendroff scheme) is indeed sufficient to maintain monotonicity and stability when simulating isotropic turbulence; and
- investigate the effects of including/excluding SGS models, i.e. compare conventional LES based on the SGS models with the ILES approach based on FDV's numerical dissipation.

This is the first FDV study to have accomplished all these objectives.

Two explicit LES SGS closures, the standard Smagorinsky and dynamic Smagorinsky SGS models, and the implicit LES based on the numerical dissipation inherent to FDV are considered. Simulations are performed on 32^3, 64^3 and 128^3 grids for the three LES closures. The effects of using higher-order elements on implicit LES computations are also examined. Both the numerical dissipation rate and the numerical viscosity due to the FDV scheme are quantified and compared, with those from the two SGS models. In addition, the FDV numerical viscosity is compared with that of the SUPG method.

The remainder of this paper is organized as follows. Section 2 presents the conservative form of the governing equations, followed by a brief description of the FDV method and the numerical viscosity formulation in Section 3. The two SGS closures used in the simulations are reviewed in Section 4. Discussion of the simulation results obtained for the test cases involving freely decaying incompressible isotropic turbulence is presented in Section 5. Finally, conclusions are drawn in Section 6.

2. Governing equations

The governing equations describing compressible, viscous fluid flow are the equations for mass, momentum and energy balance. These transport equations can be written in conservative form as:

$$\partial_t \rho + \partial_j(\rho u_j) = 0 \tag{1}$$

$$\partial_t(\rho u_i) + \partial_j(\rho u_i u_j) + \partial_j(p\delta_{ij}) = \partial_j(\sigma_{ij}) \tag{2}$$

$$\partial_t(\rho e_t) + \partial_j[(\rho e_t + p)u_j] = \partial_j[-q_j + \sigma_{ij}u_i] \tag{3}$$

where ρ is the fluid density, u_i is the fluid velocity vector and p is the pressure. The symbols ∂_t and ∂_j denote the partial differential operators $\partial/\partial t$ and $/\partial x_j$, respectively. The total energy, viscous stress tensor and heat flux vector, respectively, are given by:

$$\rho e_t = \frac{p}{\gamma - 1} + \frac{1}{2}\rho u_k u_k \tag{4}$$

$$\sigma_{ij} = \mu(T)\left(\partial_j u_i + \partial_i u_j - \frac{2}{3}\partial_k u_k \delta_{ij}\right) \tag{5}$$

$$q_j = -k(T)\partial_j T \tag{6}$$

where the dynamic viscosity $\mu(T)$ is computed using Sutherland's law as:

$$\mu(T) = T^{\frac{3}{2}}\frac{1 + C}{T + C} \tag{7}$$

with $C = 0.4$. To close the governing transport equations, we use the ideal-gas equation of state given by:

$$p = \rho R T \tag{8}$$

where T is the temperature and R is the specific gas constant taken as 0.287 kJ/kg.K.

By applying a spatial low-pass filter to the Navier–Stokes equations, the small scales of turbulence are eliminated from the solution. The kernel of a spatial filter over the flow domain Ω is denoted by $G(\boldsymbol{x})$ and a filtered variable (denoted by an overbar) is defined as:

$$\bar{f}(\boldsymbol{x}, t) = \int_{\Omega} G(\boldsymbol{x} - \boldsymbol{x}') f(\boldsymbol{x}', t) d\boldsymbol{x}' \tag{9}$$

The compressible LES equations are simpler when Favre-filtered (density-weighted) variable, defined as $\tilde{\varphi} = \overline{\rho\varphi}/\bar{\rho}$, is used (Martín *et al.*, 2000). The conservative form of the filtered Navier–Stokes equations can then be written as:

$$\partial_t \bar{\rho} + \partial_j(\bar{\rho}\tilde{u}_j) = 0 \tag{10}$$

$$\partial_t(\bar{\rho}\tilde{u}_i) + \partial_j(\bar{\rho}\tilde{u}_i\tilde{u}_j) + \partial_j(\bar{p}\delta_{ij}) = \partial_j[\tilde{\sigma}_{ij} - \tau_{ij}^{sgs}] + \partial_j[\bar{\sigma}_{ij} - \tilde{\sigma}_{ij}] \tag{11}$$

$$\partial_t(\bar{\rho}\tilde{e}_t) + \partial_j[(\bar{\rho}\tilde{e}_t + \bar{p})\tilde{u}_j] = \partial_j[-\tilde{q}_j + \tilde{\sigma}_{ij}\tilde{u}_i - c_p q_j^{sgs}] + \partial_j[\tilde{q}_j - \tilde{q}_j] \tag{12}$$

Here, the filtered form of total energy, viscous stress tensor and heat flux vector is given by:

$$\bar{\rho}\tilde{e}_t = \frac{\bar{p}}{\gamma - 1} + \frac{1}{2}\bar{\rho}\tilde{u}_k\tilde{u}_k \tag{13}$$

$$\tilde{\sigma}_{ij} = \mu(\tilde{T})\left(\partial_j\tilde{u}_i + \partial_i\tilde{u}_j - \frac{2}{3}\partial_k\tilde{u}_k\delta_{ij}\right) \tag{14}$$

$$\tilde{q}_j = -k(\tilde{T})\partial_j\tilde{T}. \tag{15}$$

The resolved (large-scale) pressure is obtained from the filtered equation of state as:

$$\bar{p} = \bar{\rho} R \tilde{T} \tag{16}$$

In equation (12), c_p is the specific heat at constant pressure.

The filtering operation leads to some extra terms in equations (11) and (12) that require closure. The SGS terms physically represent the effect of the unresolved scales on the resolved scales. Vreman *et al.* (1995, 1997) performed *a priori* tests using DNS data obtained from the calculation of a mixing layer at Mach numbers in the range of 0.2 and 0.6, and concluded that neglecting the SGS terms resulting from the non-linearities of the diffusive terms in the momentum and energy equations is acceptable, especially at low Mach numbers. Therefore $\partial_j[\overline{\sigma}_{ij} - \widetilde{\sigma_{ij}}]$ in the momentum equation and $\partial_j[\overline{q}_j - \tilde{q}_j]$ in the energy equation are neglected in this study.

The SGS stress tensor and the SGS heat flux vector that both require modeling are defined as:

$$\tau_{ij}^{sgs} = \overline{\rho}\left(\widetilde{u_i u_j} - \tilde{u}_i \tilde{u}_j\right) \tag{17}$$

$$q_j^{sgs} = \overline{\rho}\left(\widetilde{u_j T} - \tilde{u}_j \tilde{T}\right) \tag{18}$$

The variations of molecular viscosity and thermal conductivity with temperature are accounted for by Sutherland's law, which are given by:

$$\mu(\tilde{T}) = \frac{C_1 \tilde{T}^{1.5}}{C_2 + \tilde{T}}, \text{and } k(\tilde{T}) = \frac{C_3 \tilde{T}^{1.5}}{C_4 + \tilde{T}} \tag{19}$$

Sutherland's coefficients are $C_1 = 1.458 \times 10^{-6}$kg/m/sK$^{1/2}$, $C_2 = 110.4$K, $C_3 = 2.495 \times 10^{-3}$kg/ms^3 K$^{3/2}$ and $C_4 = 194.0$ K for air. The above expressions in equation (19) are valid for a temperature range of 100 and 1,900 K.

3. Flowfield Dependent Variation method

The conservative form of the filtered mass, momentum and energy equations may be written as:

$$\frac{\partial \boldsymbol{U}}{\partial t} + \frac{\partial \boldsymbol{F}_i}{\partial x_i} + \frac{\partial \boldsymbol{G}_i}{\partial x_i} = 0 \tag{20}$$

where:

$$\boldsymbol{U} = \begin{bmatrix} \bar{\rho} \\ \bar{\rho}\tilde{u}_j \\ \bar{\rho}\tilde{e}_t \end{bmatrix}, \quad \boldsymbol{F}_i = \begin{bmatrix} \bar{\rho}\tilde{u}_i \\ \bar{\rho}\tilde{u}_i\tilde{u}_j + \bar{p}\delta_{ij} \\ (\bar{\rho}\tilde{e}_t + \bar{p})\tilde{u}_i \end{bmatrix}, \quad \boldsymbol{G}_i = \begin{bmatrix} 0 \\ -\widetilde{\sigma_{ij}} + \tau_{ij}^{sgs} \\ \tilde{q}_i - \tilde{u}_j\widetilde{\sigma_{ij}} + c_p q_i^{sgs} \end{bmatrix} \tag{21}$$

Here, $\boldsymbol{U}$, $\boldsymbol{F}_i$ and $\boldsymbol{G}_i$ are the vectors of filtered conserved variables, filtered convective fluxes and filtered diffusive fluxes, respectively.

Fundamentally, the FDV method may be considered as a variant of the Lax–Wendroff Scheme (LWS) that is obtained by replacing the explicit time derivatives in LWS by a weighted combination of explicit and implicit time derivatives. This is done to ensure both the numerical stability and monotonicity of FDV (Girgis *et al.*, 2015).

Performing a Taylor series expansion of $\boldsymbol{U}^{n+1}$ about $\boldsymbol{U}^{n}$ gives:

$$\boldsymbol{U}^{n+1} = \boldsymbol{U}^{n} + \Delta t\frac{\partial \boldsymbol{U}^{n}}{\partial t} + \frac{\Delta t^{2}}{2}\frac{\partial^{2}\boldsymbol{U}^{n}}{\partial t^{2}} + O(\Delta t^{3}) \tag{22}$$

where Δt is the time step between solutions $\boldsymbol{U}^{n}/\boldsymbol{U}^{n+1}$ and n denotes the time index. Replacing the explicit time derivatives in equation (22) by a weighted explicit-implicit combination of FDV parameters, s_a and s_b, yields:

$$\begin{aligned}\boldsymbol{U}^{n+1} = \boldsymbol{U}^{n} + \Delta t\left[(1 - s_a)\frac{\partial \boldsymbol{U}^{n}}{\partial t} + s_a\frac{\partial \boldsymbol{U}^{n+1}}{\partial t}\right] \\ + \frac{\Delta t^{2}}{2}\left[(1 - s_b)\frac{\partial^{2}\boldsymbol{U}^{n}}{\partial t^{2}} + s_b\frac{\partial^{2}\boldsymbol{U}^{n+1}}{\partial t^{2}}\right] + O(\Delta t^{3})\end{aligned} \tag{23}$$

where $0 \le s_a \le 1$ and $0 \le s_b \le 1$. These FDV parameters act as weighting functions between explicit and implicit methods. If $s_a = s_b = 0$ (e.g. in the regions of zero gradients in a Flowfield), the method is fully explicit as in LWS, whereas if $s_a = s_b = 1$ (e.g. in the regions of high gradients in flow variables), the method becomes fully implicit.

Rearranging equation (20) by separating the time and the spatial derivatives, one obtains:

$$\frac{\partial \boldsymbol{U}}{\partial t} = -\frac{\partial \boldsymbol{F}_i}{\partial x_i} - \frac{\partial \boldsymbol{G}_i}{\partial x_i} \tag{24}$$

Taking a time derivative of equation (24), interchanging spatial and time derivatives, and recognizing that $\boldsymbol{F}_i = \boldsymbol{F}_i(\boldsymbol{U})$, and $\boldsymbol{G}_i = \boldsymbol{G}_i(\boldsymbol{U},\boldsymbol{U}_j)$, where $\boldsymbol{U}_j = \partial \boldsymbol{U}/\partial x_j$, yields:

$$\frac{\partial^{2}\boldsymbol{U}}{\partial t^{2}} = \frac{\partial}{\partial x_i}\left[(\boldsymbol{a}_i + \boldsymbol{b}_i)\left\{\frac{\partial \boldsymbol{F}_j}{\partial x_j} + \frac{\partial \boldsymbol{G}_j}{\partial x_j}\right\}\right] + \frac{\partial^{2}}{\partial x_i \partial x_j}\left[\boldsymbol{c}_{ij}\left\{\frac{\partial \boldsymbol{F}_k}{\partial x_k} + \frac{\partial \boldsymbol{G}_k}{\partial x_k}\right\}\right] \tag{25}$$

Here:

$$\boldsymbol{a}_i = \frac{\partial \boldsymbol{F}_i}{\partial \boldsymbol{U}}, \quad \boldsymbol{b}_i = \frac{\partial \boldsymbol{G}_i}{\partial \boldsymbol{U}}, \quad \boldsymbol{c}_{ij} = \frac{\partial \boldsymbol{G}_i}{\partial \boldsymbol{U}_j} \tag{26}$$

where $\boldsymbol{a}_i$, $\boldsymbol{b}_i$ and $\boldsymbol{c}_{ij}$ are the Jacobians of convection, diffusion and diffusion gradient, respectively.

Substituting equations (24) and (25) into equation (23), and neglecting the product of $\boldsymbol{c}_{ij}$ with the third-order spatial derivatives of $\boldsymbol{F}_k$ and $\boldsymbol{G}_k$ gives:

$$\begin{aligned}\Delta \boldsymbol{U}^{n+1} = \Delta t\left[\left\{-\frac{\partial \boldsymbol{F}_i^{n}}{\partial x_i} - \frac{\partial \boldsymbol{G}_i^{n}}{\partial x_i}\right\} + s_a\left\{-\frac{\partial \Delta \boldsymbol{F}_i^{n+1}}{\partial x_i} - \frac{\partial \Delta \boldsymbol{G}_i^{n+1}}{\partial x_i}\right\}\right] \\ + \frac{\Delta t^{2}}{2}\frac{\partial}{\partial x_i}\left[(\boldsymbol{a}_i + \boldsymbol{b}_i)\left\{\frac{\partial \boldsymbol{F}_j^{n}}{\partial x_j} + \frac{\partial \boldsymbol{G}_j^{n}}{\partial x_j}\right\}\right] \\ + \frac{\Delta t^{2}}{2}s_b\frac{\partial}{\partial x_i}\left[(\boldsymbol{a}_i + \boldsymbol{b}_i)\left\{\frac{\partial \Delta \boldsymbol{F}_j^{n+1}}{\partial x_j} + \frac{\partial \Delta \boldsymbol{G}_j^{n+1}}{\partial x_j}\right\}\right],\end{aligned} \tag{27}$$

where $\Delta \boldsymbol{U}^{n+1} = \boldsymbol{U}^{n+1} - \boldsymbol{U}^{n}$, $\Delta \boldsymbol{F}^{n+1} = \boldsymbol{F}^{n+1} - \boldsymbol{F}^{n}$ and $\Delta \boldsymbol{G}^{n+1} = \boldsymbol{G}^{n+1} - \boldsymbol{G}^{n}$.

To treat the effects of the FDV parameters on convection and diffusion terms separately, s_a and s_b are split into $s_{a,\mathrm{conv}}/s_{a,\mathrm{diff}}$ and $s_{b,\mathrm{conv}}/s_{b,\mathrm{diff}}$, respectively, and reassigned as follows:

$$\mathrm{s_a}\Delta \boldsymbol{F}_i \Rightarrow s_{a,\mathrm{conv}}\Delta \boldsymbol{F}_i, \quad \mathrm{s_a}\Delta \boldsymbol{G}_i \Rightarrow s_{a,\mathrm{diff}}\Delta \boldsymbol{G}_i \tag{28}$$

$$\mathrm{s_b}\Delta \boldsymbol{F}_i \Rightarrow s_{b,\mathrm{conv}}\Delta \boldsymbol{F}_i, \quad \mathrm{s_b}\Delta \boldsymbol{G}_i \Rightarrow s_{b,\mathrm{diff}}\Delta \boldsymbol{G}_i \tag{29}$$

Physical roles are assigned to these implicitness parameters when their values are calculated from appropriate flow quantities such as Mach number (M) for convection and Reynolds number (Re) for diffusion. The first-order FDV parameters, $s_{a,\mathrm{conv}}$ and $s_{a,\mathrm{diff}}$, are Flowfield-dependent, while the second-order parameters, $s_{b,\mathrm{conv}}$ and $s_{b,\mathrm{diff}}$, are assumed to have a power-law dependence on the first-order parameters as follows:

$$s_{a,\mathrm{conv}} = \begin{cases} \min(r, 1) & r > \alpha \\ 0 \quad r > \alpha, & M_{\min} \neq 0 \\ 1 & M_{\min} = 0 \end{cases} \tag{30}$$

$$s_{b,\mathrm{conv}} = \frac{1}{2}(1 + s_{a,\mathrm{conv}}^{\eta}) \tag{31}$$

where $r = \sqrt{M_{\max}^2 - M_{\min}^2}/M_{\min}$

$$s_{a,\mathrm{diff}} = \begin{cases} \min(r, 1) & r > \alpha \\ 0 \quad r < \alpha, & Re_{\min} \neq 0 \\ 1 & Re_{\min} = 0 \end{cases} \tag{32}$$

$$s_{b,\mathrm{diff}} = \frac{1}{2}(1 + s_{a,\mathrm{diff}}^{\eta}) \tag{33}$$

where $r = \sqrt{Re_{\max}^2 - Re_{\min}^2}/Re_{\min}$

The maximum and minimum values of M and Re are calculated from the nodal values within the element, and the parameters $\alpha = 0.001$ and $\eta = 0.1$ are used in this study. The modification to the variation parameters, $\mathrm{s_a}$ and $\mathrm{s_b}$, assists in maintaining the second-order temporal accuracy of the method and in adding stability to flows with stronger shocks (Richardson *et al.*, 2010). All the FDV parameters are updated at each time step.

Rewriting equation (27) in terms of FDV parameters $s_{a,\mathrm{conv}}$, $s_{a,\mathrm{diff}}$ and $s_{b,\mathrm{diff}}$, $s_{b,\mathrm{diff}}$ yields:

$$\begin{aligned} \Delta \boldsymbol{U}^{n+1} = & -\Delta t\left[\left\{\frac{\partial \boldsymbol{F}_i^n}{\partial x_i} + \frac{\partial \boldsymbol{G}_i^n}{\partial x_i}\right\} + \left\{s_{a,\mathrm{conv}}\frac{\partial \Delta \boldsymbol{F}_i^{n+1}}{\partial x_i} + s_{a,\mathrm{diff}}\frac{\partial \Delta \boldsymbol{G}_i^{n+1}}{\partial x_i}\right\}\right] \\ & + \frac{\Delta t^2}{2}\frac{\partial}{\partial x_i}\left[(\boldsymbol{a}_i + \boldsymbol{b}_i)\left\{\frac{\partial \boldsymbol{F}_j^n}{\partial x_j} + \frac{\partial \boldsymbol{G}_j^n}{\partial x_j}\right\}\right] \\ & + \frac{\Delta t^2}{2}\frac{\partial}{\partial x_i}\left[(\boldsymbol{a}_i + \boldsymbol{b}_i)\left\{s_{b,\mathrm{conv}}\frac{\partial \Delta \boldsymbol{F}_j^{n+1}}{\partial x_j} + s_{b,\mathrm{diff}}\frac{\partial \Delta \boldsymbol{G}_j^{n+1}}{\partial x_j}\right\}\right] \end{aligned} \tag{34}$$

Replacing $\Delta \boldsymbol{F}_j^{n+1}$ and $\Delta \boldsymbol{G}_j^{n+1}$ with their respective Jacobians stated in equation (26), one obtains:

$$\left[\boldsymbol{I} + \boldsymbol{D}_i\frac{\partial}{\partial x_i} + \boldsymbol{E}_{ij}\frac{\partial^2}{\partial x_i \partial x_j}\right]\Delta \boldsymbol{U}^{n+1} = \boldsymbol{Q}^n \tag{35}$$

where $\boldsymbol{I}$ is the identity matrix.

Finally, writing equation (34) in residual form gives the following expression:

$$\boldsymbol{R} = \Delta \boldsymbol{U}^{n+1} + \boldsymbol{D}_i^n \Delta \boldsymbol{U}_{,i}^{n+1} + \boldsymbol{E}_{ij}^n \Delta \boldsymbol{U}_{,ij}^{n+1} - \boldsymbol{Q}^n = O(\Delta t^3) \tag{36}$$

such that:

$$\boldsymbol{D}_i^n = \Delta t(s_{\mathrm{a,conv}}\boldsymbol{a}_i + s_{\mathrm{a,diff}}\boldsymbol{b}_i) \tag{37}$$

$$\boldsymbol{E}_{ij}^n = \Delta t s_{\mathrm{a,diff}}\boldsymbol{c}_{ij} - \frac{\Delta t^2}{2}[(\boldsymbol{a}_i + \boldsymbol{b}_i)(s_{\mathrm{b,conv}}\boldsymbol{a}_j + s_{\mathrm{b,diff}}\boldsymbol{b}_j)] \tag{38}$$

$$\boldsymbol{Q}^n = \Delta t(\boldsymbol{F}_{i,i}^n + \boldsymbol{G}_{i,i}^n) - \frac{\Delta t^2}{2}(\boldsymbol{a}_i + \boldsymbol{b}_i)(\boldsymbol{F}_{j,ji}^n + \boldsymbol{G}_{j,ji}^n) \tag{39}$$

Because all the numerical stability mechanisms are already built into the FDV method using the implicitness parameters, the finite element discretization via the standard Galerkin method is sufficient:

$$\int_\Omega \Phi_\alpha \boldsymbol{R}(\boldsymbol{U}, \boldsymbol{F}_i, \boldsymbol{G}_i)d\Omega = 0 \tag{40}$$

where Φ_α is a shape function corresponding to the node with global index α. Applying the standard Galerkin method stated in equation (40) to the residual given in equation (36), integrating by parts, and arranging in a compact form, the global form of the assembled finite element equations are given by:

$$(A_{\alpha\beta rs}^n + B_{\alpha\beta rs}^n)\Delta U_{\beta s}^{n+1} = H_{\alpha r}^n + N_{\alpha r}^n \tag{41}$$

where:

$$A_{\alpha\beta rs}^n = \int_\Omega (\Phi_\alpha \Phi_\beta \delta_{rs} - \Phi_{\alpha,i}\Phi_\beta D_{irs}^n - \Phi_{\alpha,i}\Phi_{\beta,j}E_{ijrs}^n)d\Omega \tag{42}$$

$$B_{\alpha\beta rs}^n = \int_\Gamma \left(\overset{*}{\Phi}_\alpha \overset{*}{\Phi}_\beta \overset{*}{D}{}_{irs}^n + \overset{*}{\Phi}_\alpha \overset{*}{\Phi}_{\beta,j} \overset{*}{E}{}_{ijrs}^n\right)n_i d\Gamma \tag{43}$$

$$H_{\alpha r}^n = \int_\Omega \left(\Delta t \Phi_{\alpha,i}(F_{ir}^n + G_{ir}^n) - \frac{\Delta t^2}{2}\Phi_{\alpha,i}(a_{irs} + b_{irs})(F_{js,j}^n + G_{js,j}^n)\right)d\Omega \tag{44}$$

$$N_{\alpha r}^n = \int_\Gamma \left(-\Delta t \overset{*}{\Phi}_\alpha \left(\overset{*}{F}{}_{ir}^n + \overset{*}{G}{}_{ir}^n\right) + \frac{\Delta t^2}{2}\overset{*}{\Phi}_\alpha (a_{irs} + b_{irs})\left(\overset{*}{F}{}_{js,j}^n + \overset{*}{G}{}_{js,j}^n\right)\right)n_i d\Gamma \tag{45}$$

In equations (42)-(45), α and β denote the global nodal indices; $r,s = 1, 2, \ldots, 5$ are the indices for the five conserved variables; $i, j = 1, 2, 3$ are the physical coordinate indices; δ_{rs} represents

the Kronecker delta; the superscript * represents the variable along the inter-element contour; the integral over Ω and Γ denote the element and contour integral, respectively; and n_i is the normal to the element surface. The contour integrals of equations (43) and (45) cancel each other along inter-element boundaries, thereby ensuring flux conservation. Neumann boundary conditions can be imposed through these contour integrals, while Dirichlet boundary conditions can be enforced through element-by-element discretization approach.

3.1 Numerical viscosity of the FDV method

In this section, an expression for the numerical viscosity inherent to the FDV scheme is derived. Because the numerical dissipation arises primarily from the convective terms, only the Euler form of the governing equations is considered for the derivation. The Euler form of the filtered momentum equations are given by:

$$\frac{\partial(\bar{\rho}\tilde{u}_i)}{\partial t} + \frac{\partial(\bar{\rho}\tilde{u}_i\tilde{u}_j)}{\partial x_j} = 0 \tag{46}$$

Taking the time derivative of equation (46), and rearranging, one obtains:

$$\frac{\partial^2(\bar{\rho}\tilde{u}_i)}{\partial t^2} = \frac{\partial}{\partial t}\left[-\frac{\partial(\bar{\rho}\tilde{u}_i\tilde{u}_j)}{\partial x_j}\right] = -\frac{\partial}{\partial x_j}\left[\frac{\partial(\bar{\rho}\tilde{u}_i\tilde{u}_j)}{\partial t}\right] \tag{47}$$

Differentiating the right-hand side of equation (47) by product rule, and using equation (46) yields:

$$\frac{\partial^2(\bar{\rho}\tilde{u}_i)}{\partial t^2} = \frac{\partial}{\partial x_j}\left[\tilde{u}_j\left\{\bar{\rho}\tilde{u}_i\frac{\partial\tilde{u}_k}{\partial x_k} + \tilde{u}_k\frac{\partial(\bar{\rho}\tilde{u}_i)}{\partial x_k}\right\}\right] \tag{48}$$

which can be written as:

$$\frac{\partial^2(\bar{\rho}\tilde{u}_i)}{\partial t^2} = \frac{\partial}{\partial x_j}\left[\bar{\rho}\tilde{u}_j\tilde{u}_i\frac{\partial\tilde{u}_k}{\partial x_k}\right] + \frac{\partial}{\partial x_j}\left[\tilde{u}_j\tilde{u}_k\frac{\partial(\bar{\rho}\tilde{u}_i)}{\partial x_k}\right] \tag{49}$$

Rewriting equation (49) in tensorial form gives:

$$\frac{\partial^2(\bar{\rho}\tilde{u}_i)}{\partial t^2} = \nabla\cdot\left[(\bar{\rho}\tilde{u}_j\tilde{u}_i)\{\nabla\cdot\tilde{\boldsymbol{u}}\}\right] + \nabla\cdot\left[\tilde{u}_j\tilde{u}_k\cdot\nabla(\bar{\rho}\tilde{\boldsymbol{u}})\right] \tag{50}$$

Recalling that the numerical diffusion term may be expressed in the tensorial form as $[\nabla\cdot(\boldsymbol{D}\cdot\nabla(\bar{\rho}\tilde{\boldsymbol{u}}))]$; it can be recognized that the first term on the right-hand side of equation (50) is not a diffusion term, and that the second term provides the numerical diffusion in FDV. Equation (50) can be approximated by:

$$\frac{\partial^2(\bar{\rho}\tilde{u}_i)}{\partial t^2} \approx \nabla\cdot[(\tilde{\boldsymbol{u}}\tilde{\boldsymbol{u}})\cdot\nabla(\bar{\rho}\tilde{\boldsymbol{u}})] = \frac{\partial}{\partial x_j}\left[\tilde{u}_j\tilde{u}_k\frac{\partial(\bar{\rho}\tilde{u}_i)}{\partial x_k}\right] \tag{51}$$

Performing a Taylor series expansion of $(\bar{\rho}\tilde{u}_i)^{n+1}$ about $(\bar{\rho}\tilde{u}_i)^n$ gives:

$$(\overline{\rho}\tilde{u}_i)^{n+1} = (\overline{\rho}\tilde{u}_i)^n + \Delta t\frac{\partial(\overline{\rho}\tilde{u}_i)^n}{\partial t} + \frac{\Delta t^2}{2}\frac{\partial^2(\overline{\rho}\tilde{u}_i)^n}{\partial t^2} + O(\Delta t^3) \tag{52}$$

Replacing the explicit time derivatives in equation (52) by a weighted explicit–implicit combination using the convective FDV parameters, $s_{a,conv}$ and $s_{b,conv}$, and writing $\Delta(\overline{\rho}\tilde{u}_i)^{n+1} = (\overline{\rho}\tilde{u}_i)^{n+1} - (\overline{\rho}\tilde{u}_i)^n$ yields:

$$\begin{aligned}\Delta(\overline{\rho}\tilde{u}_i)^{n+1} = \Delta t\left[(1 - s_{a,conv})\frac{\partial(\overline{\rho}\tilde{u}_i)^n}{\partial t} + s_{a,conv}\frac{\partial(\overline{\rho}\tilde{u}_i)^{n+1}}{\partial t}\right] \\ + \frac{\Delta t^2}{2}\left[(1 - s_{b,conv})\frac{\partial^2(\overline{\rho}\tilde{u}_i)^n}{\partial t^2} + s_{b,conv}\frac{\partial^2(\overline{\rho}\tilde{u}_i)^{n+1}}{\partial t^2}\right]\end{aligned} \tag{53}$$

Substituting equations (46) and (51) into equation (53), and recognizing that the second-order time derivatives contain the numerical diffusion terms, one obtains:

$$\frac{\Delta(\overline{\rho}\tilde{u}_i)^{n+1}}{\Delta t} \approx \frac{\Delta t}{2}\left[(1 - s_{b,conv})\left\{\frac{\partial}{\partial x_j}\left[u_j u_k\frac{\partial(\overline{\rho}\tilde{u}_i)}{\partial x_k}\right]\right\}^n + s_{b,conv}\left\{\frac{\partial}{\partial x_j}\left[u_j u_k\frac{\partial(\overline{\rho}\tilde{u}_i)}{\partial x_k}\right]\right\}^{n+1}\right] \tag{54}$$

The numerical viscosity tensor can be quantified from the coefficients of the second-order spatial derivatives given in equation (54) and is expressed as:

$$\nu_{FDV,jk} = \frac{\Delta t}{2}[\tilde{u}_j\tilde{u}_k] = \frac{1}{2}C\Delta x|\tilde{\boldsymbol{u}}|\tilde{u}_j^*\tilde{u}_k^* \tag{55}$$

where the Courant number $C = \Delta t|\tilde{\boldsymbol{u}}|/\Delta x$, $|\tilde{\boldsymbol{u}}|$ is the magnitude of the velocity vector, and $\tilde{u}_j^* = \tilde{u}_j/|\tilde{\boldsymbol{u}}|$ is a scaled velocity. It should be noted that the FDV numerical viscosity ν_{FDV} is a second-order tensor. One can therefore use a lower dimensional quantification of ν_{FDV} by considering its Frobenius norm given by $\|\nu_{FDV}\|_F = \sqrt{\Sigma_{j=1}^3\,\Sigma_{k=1}^3\,\nu_{FDV,jk}}$.

3.2 Numerical viscosity of the SUPG method

In addition to comparing FDV ILES with conventional LES based on the standard Smagorinsky and dynamic Smagorinsky models, we compare the numerical viscosity of FDV with that of SUPG FEM. In the seminal SUPG study of Brooks and Hughes (1982), the following form was provided for the added numerical diffusivity on a uniform hexahedral grid:

$$\nu_{SUPG,jk} = \frac{1}{\sqrt{15}}\Delta x(\bar{\xi}\tilde{u}_1 + \bar{\eta}\tilde{u}_2 + \bar{\zeta}\tilde{u}_3)\tilde{u}_j^*\tilde{u}_k^* \tag{56}$$

where the parameters $\bar{\xi}, \bar{\eta}$, and $\bar{\zeta}$ are based on the cell Peclet or Reynolds number; $\tilde{u}_1 = \tilde{\boldsymbol{u}}\cdot e_1$, $\tilde{u}_2 = \tilde{\boldsymbol{u}}\cdot e_2$, and $\tilde{k}_3 = \tilde{\boldsymbol{u}}\cdot e_3$ are designed so that the numerical viscosity is only active along the principal flow direction (hence, streamline upwind). When solving Euler equations, as in the current study, the cell Reynolds number $Re \to \infty$, for which the parameters $\bar{\xi}, \bar{\eta}$, and $\bar{\zeta}$ are all unity. Therefore, we obtain:

$$\nu_{SUPG,jk} = \frac{1}{\sqrt{15}}\Delta x|\tilde{u}_1 + \tilde{u}_2 + \tilde{u}_3|\tilde{u}_j^*\tilde{u}_k^* \tag{57}$$

where we consider $|\tilde{u}_1 + \tilde{u}_2 + \tilde{u}_3|$ to ensure positive numerical viscosity (Brooks and Hughes, 1982). One can notice a striking similarity between the FDV and SUPG formulations for the numerical viscosity. For instance, when Courant number $C = 2|\tilde{u}_1 + \tilde{u}_2 + \tilde{u}_3|/(\sqrt{15}|\tilde{u}|)$, the two methods would provide identical diffusion. We will quantify ν_{SUPG} by considering its Frobenius norm, as indicated above for ν_{FDV}.

3.3. Numerical dissipation rate of the FDV method

The numerical dissipation rate in the filtered momentum equation can be estimated as (Garnier *et al.*, 1999):

$$\varepsilon_{num} = \langle \tilde{u}_i \partial_j \mathcal{F}_{ij}^{FDV} \rangle \tag{58}$$

where:

$$F_{ij}^{FDV} = (\bar{\rho}\tilde{u}_i \tilde{u}_j + \delta_{ij}\bar{p}) \tag{59}$$

Here, F_{ij}^{FDV} is the filtered convective flux in the momentum equation. It may be noted that the FDV parameters act on the momentum equation and the continuity and energy equations. Nevertheless, only the contribution from the momentum equation is considered in the calculation of the numerical dissipation rate to enable direct comparison with the SGS dissipation rate [see equation (69)].

4. Subgrid-scale closures

The SGS closures considered are the standard Smagorinsky and dynamic Smagorinsky models.

4.1 Smagorinsky model

The first SGS model was developed for incompressible flows by Smagorinsky (1963) based on an eddy-viscosity assumption, which implies that the turbulent kinetic energy production of the small-scale structures is balanced by the SGS dissipation. The model relates the turbulent eddy-viscosity as a function of resolved velocity field as:

$$\nu_{sgs} = (C_s\overline{\Delta})^2|\tilde{S}| = (C_s\overline{\Delta})^2(2\tilde{S}_{ij}\tilde{S}_{ij})^{1/2} \tag{60}$$

where C_s is the Smagorinsky constant, $\overline{\Delta}$ is the width of the grid filter, $\tilde{S}_{ij} = 1/2(\partial_j\tilde{u}_i + \partial_i\tilde{u}_j)$ is the filtered strain-rate tensor and $|\tilde{S}| = (2\tilde{S}_{ij}\tilde{S}_{ij})^{1/2}$ is its norm. The filter width is calculated as $\overline{\Delta} = (\overline{\Delta}_x\overline{\Delta}_y\overline{\Delta}_z)^{1/3}$, where $\overline{\Delta}_x$, $\overline{\Delta}_y$, and $\overline{\Delta}_z$ are the grid sizes in the x-, y- and z-directions, respectively. This model is valid only if the filter width is in the inertial subrange. The SGS stress tensor in equation (17) is modeled for compressible flows using the modification proposed by Moin *et al.* (1991) to the dynamic eddy-viscosity model of Germano *et al.* (1991) for incompressible flows, and is given by:

$$\tau_{ij}^{sgs} - \frac{1}{3}\tau_{kk}^{sgs}\delta_{ij} = -2\bar{\rho}\nu_{sgs}\left(\tilde{S}_{ij} - \frac{1}{3}\tilde{S}_{kk}\delta_{ij}\right) \tag{61}$$

In this study, the trace of the SGS stress tensor τ_{kk}^{sgs} is neglected as proposed by Erlebacher *et al.* (1992). They conjected that for turbulent Mach number $M_t < 0.4$, the effect of τ_{kk}^{sgs} is negligible; their DNS of isotropic turbulence confirmed this conjecture. Vreman *et al.* (1997)

confirmed the above findings with their simulation of 3-D compressible mixing layers at a mean convective Mach number of 0.2. In their *a priori* test, the SGS model that neglects τ_{kk}^{sgs} was found to be in better agreement with DNS results. To complete the closure of this model, the SGS heat flux vector given in equation (18) is modeled using the eddy-diffusivity model and a constant turbulent Prandtl number as:

$$q_i^{sgs} = -\overline{\rho}\frac{\nu_{sgs}}{\mathrm{Pr}_t}\frac{\partial \widetilde{T}}{\partial x_i} \tag{62}$$

4.2 Dynamic Smagorinsky model

To adapt the Smagorinsky constant to local structure of the flow, Germano *et al.* (1991) proposed an algorithm that enables the computation of a time- and space-dependent coefficient. Their original proposal for incompressible flows was later extended by Moin *et al.* (1991) for compressible applications. The dynamic model is based on self-similarity of the inertial range of the kinetic energy spectrum at different length scales. Therefore, the same functional form for the SGS quantities can be assumed at the grid length scale $\overline{\Delta}$ representative of the computational grid and at a larger test filter length scale $\hat{\Delta}$. Details of the derivation can be found in Germano *et al.* (1991) and Moin *et al.* (1991). The residual stress at the test filter level T_{ij} appears when the test filter is applied to the grid-filtered Navier–Stokes equations. An identity due to Germano *et al.* (1991) is then obtained by applying the test filter on the residual stresses at the grid filter level τ_{ij}^{sgs} and subtracting the resulting expression from T_{ij} thus:

$$\mathcal{L}_{ij} = T_{ij} - \tau_{ij}^{sgs} = \widehat{\overline{\rho}\widetilde{u}_i\widetilde{u}_j} - (1/\hat{\overline{\rho}})\widehat{\overline{\rho}\widetilde{u}_i}\widehat{\overline{\rho}\widetilde{u}_j} \tag{63}$$

Assuming that the same functional form, as in Smagorinsky model, could be used for the residual stresses at both levels, the modeled forms are:

$$\tau_{ij}^{sgs} - \frac{1}{3}\tau_{kk}^{sgs}\delta_{ij} = -2C_d\overline{\Delta}^2\overline{\rho}\,|\widetilde{S}|\left(\widetilde{S}_{ij} - \frac{1}{3}\widetilde{S}_{kk}\delta_{ij}\right) \tag{64}$$

and:

$$T_{ij} - \frac{1}{3}T_{kk}\delta_{ij} = -2C_d\hat{\overline{\Delta}}^2\hat{\overline{\rho}}\,|\hat{\widetilde{S}}|(\hat{\widetilde{S}}_{ij} - \frac{1}{3}\hat{\widetilde{S}}_{kk}\delta_{ij}) \tag{65}$$

Substituting equations (64) and (65) into equation (63), the modeled expression for deviatoric part of Leonard stress tensor $\mathcal{L}_{ij}^d$ is obtained as:

$$\mathcal{L}_{ij}^d = \mathcal{L}_{ij} - \frac{1}{3}\mathcal{L}_{kk}\delta_{ij} = C_d\overline{\Delta}^2 M_{ij} \tag{66}$$

where M_{ij} is defined as:

$$M_{ij} = 2\overline{\rho}\,|\widetilde{S}|\left(\widetilde{\widetilde{S}_{ij}} - \frac{1}{3}\widetilde{S}_{kk}\delta_{ij}\right) - 2\left(\frac{\hat{\overline{\Delta}}}{\overline{\Delta}}\right)^2\hat{\overline{\rho}}\,|\hat{\widetilde{S}}|\left(\hat{\widetilde{S}}_{ij} - \frac{1}{3}\hat{\widetilde{S}}_{kk}\delta_{ij}\right) \tag{67}$$

Finally, using a least-squares minimization procedure as per Lilly (1992), one obtains:

$$C_d\overline{\Delta}^2 = \frac{\left\langle (\mathscr{L}_{ij} - \frac{1}{3}\mathscr{L}_{kk}\delta_{ij})M_{ij} \right\rangle}{\langle M_{kl}M_{kl} \rangle} \tag{68}$$

This procedure gives a local time-dependent estimate of the model coefficient $C_d\overline{\Delta}^2$, which is updated at each time iteration. The quantities enclosed by angled brackets $\langle \cdot \rangle$ indicate that spatial averaging is to be performed over homogeneous directions. This is done to prevent numerical instabilities due to potential negative values of C_d or certain quantities from vanishing which could invalidate the evaluation of the model coefficient. The only adjustable parameter inherent to the model is the filter width ratio $\hat{\overline{\Delta}}/\overline{\Delta}$ taken as 2 in this study. The dynamic procedure requires the definition of an explicit low-pass filter for the test-filtering operation. The finite element-based test filter used in the dynamic algorithm is a generalized top-hat filter arising from Gaussian quadrature rule approximations. Detailed description of this test filter can be found in Tejada-Martínez and Jansen (2003, 2004).

4.3 SGS dissipation rate

Garnier *et al.* (1999) proposed an expression for estimating the SGS dissipation rate for incompressible flows as:

$$\varepsilon_{sgs} = \langle \tilde{u}_i \partial_j \tau_{ij}^{sgs} \rangle \tag{69}$$

where,

$$\tau_{ij}^{sgs} = -2\bar{\rho}\nu_{sgs}\tilde{S}_{ij} \tag{70}$$

5. Results and discussion

This section presents the results from the simulations of freely decaying, inviscid isotropic turbulence. The Euler form of decaying isotropic turbulence is commonly used when one is interested in isolating and quantifying numerical dissipation (Garnier *et al.*, 1999; Ciardi *et al.*, 2005; Thornber *et al.*, 2007; Bidadi and Rani, 2015). The numerical viscosity and dissipation rate inherent to the FDV scheme are quantified and compared with the corresponding quantities for the standard Smagorinsky and dynamic Smagorinsky SGS models. Also presented are comparisons of the FDV numerical and SGS eddy-viscosities with the SUPG numerical viscosity.

5.1 Flow initialization

For all the cases considered in the study, the flow domain is initialized with a random divergence-free velocity field, and constant density and temperature fields. The computational domain is a periodic cubic box of size 2π. The 3-D velocity field is initialized such that it satisfies the kinetic energy spectrum $E(k)$ given by (Samtaney *et al.*, 2001):

$$E(k) = Ak^4 \exp[-2(k/k_p)^2] \tag{71}$$

where k is the wave number, k_p is the wave number at which $E(k)$ peaks ($k_p = 4$) and A is a constant chosen to get a specified initial turbulent kinetic energy ($A = 0.0145$). The initial energy spectrum is applied within the prescribed wave number range $1 \leq k \leq 10$. The initial turbulent Mach number $M_{t0} = 0.05$ for all the cases, so that the flow may be considered essentially incompressible. A constant time step $\Delta t = 10^{-3}$ is used for the computations.

Simulations were performed for three grid resolutions 32^3, 64^3 and 128^3, and were run up to a normalized time $t^* = 10$, which corresponds to approximately three large-scale eddy-turnover times. Here, $t^* = t/\tau$ with $\tau = k_0/\varepsilon_0$, where k_0 and ε_0 are turbulent kinetic energy and dissipation rate at the initial conditions, respectively.

Figure 1 shows the Q-criterion iso-surfaces colored by the vorticity magnitude at two computational times, $t^* = 0$ and $t^* = 1$. The iso-surfaces shown are for implicit LES on the 128^3 grid with second-order accurate FDV scheme. The Q-criterion is defined as:

$$Q = \frac{1}{2}(\tilde{R}_{ij}\tilde{R}_{ij} - \tilde{S}_{ij}\tilde{S}_{ij}) \tag{72}$$

where $\tilde{R}_{ij}$ is the filtered rotational-rate tensor given by $\tilde{R}_{ij} = (\partial\tilde{v}_i/\partial x_j - \partial\tilde{v}_j/\partial x_i)$ and $\tilde{S}_{ij}$ is the filtered strain-rate tensor. It is evident from Figure 1(a) that the initial flowfield is characterized by eddies corresponding to low wavenumber modes. In Figure 1(b), the Q-criterion iso-surfaces are shown at $t^* = 1$. The multitude of scales, as well as the presence of worm-like vortex structures, suggests that the turbulent kinetic energy has cascaded down to the high wavenumber modes or the small-scale structures. At later computational times ($t^* > 1$), the small-scale vortices dissipate their energy, and in the process, coalesce into a fewer number of large structures.

5.2 Implicit LES computations

In this section, we present the temporal and spectral statistics of decaying isotropic turbulence obtained from the implicit LES runs, i.e. without any explicit SGS model, at three grid resolutions. Second-order piecewise linear hexahedral elements are used for spatial discretization, while time integration is achieved through fully-implicit iterative time-marching procedure based on the Generalized Minimal RESidual (GMRES) algorithm.

Figure 2(a), 2(b) and 2(c) presents a comparison of resolved kinetic energy spectra for the ILES case at different computational times on the 32^3, 64^3 and 128^3 grids, respectively. The resolved kinetic energy, initially confined to the $1 \leq k \leq 10$ wavenumber range, is transferred to higher wavenumbers due to the nonlinear energy cascade process. Ideally, the energy spectrum in the inertial range should have a slope of $-5/3$ on log-log axes, as predicted by

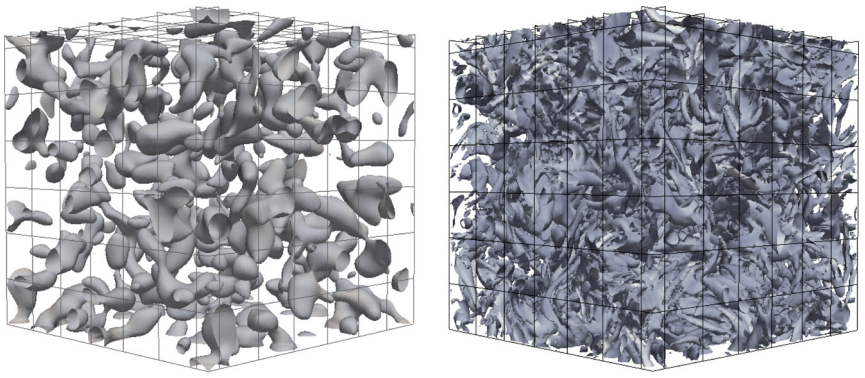

(a) **(b)**

Figure 1.
Q-criterion iso-surfaces colored by vorticity magnitude at two computational times on the 128^3 grid: (a) $t^* = 0$, and (b) $t^* = 1$

Note: Figures correspond to the implicit LES case with second-order accurate FDV method

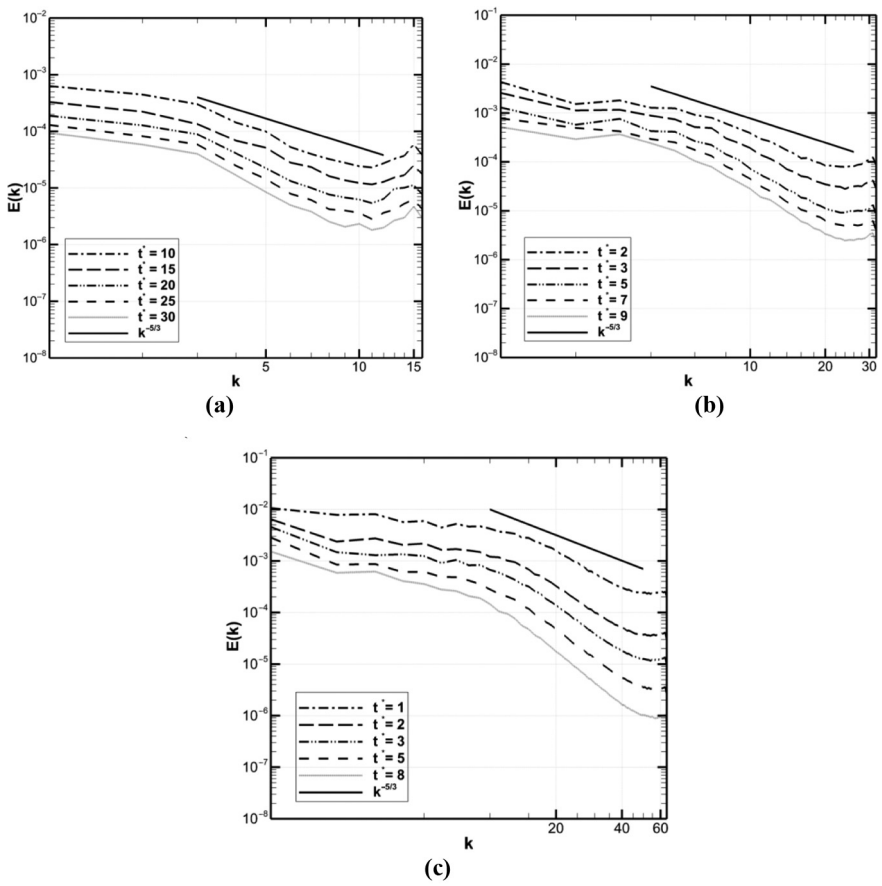

Figure 2.
Comparison of resolved kinetic energy spectra with the − 5/3 power law at different computational times for: (a) 32^3, (b) 64^3 and (c) 128^3 grids

Note: Results are for implicit LES case with second-order accurate FDV method

Kolmogorov (1941a). For all the grid resolutions considered, the energy spectra show reasonable agreement with the $k^{-5/3}$ scaling in the inertial range. Thus, the FDV-ILES framework tends to capture the Kolmogorov scaling, although an under-dissipative behavior is observed at high wavenumbers close to the cutoff wavenumber k_c. It should be noted that as the grid resolution increases, the cutoff wavenumber increases and the energy build-up close to the cutoff wavenumber reduces. The spectral energy increases with grid resolution at all wavenumbers.

Theoretically, the decay rate of kinetic energy in decaying isotropic turbulence scales with time as t^{*-n} (Pope, 2000). In prior studies, decay exponent values ranging between $n = 1.2$ and 1.43 were reported (Oberlack, 2002; Yakhot, 2004; Kolmogorov, 1941b). Figure 3 shows the time history of the resolved kinetic energy on the 32^3, 64^3 and 128^3 grids. During the initial transient stage, the kinetic energy is being transferred from low to high wavenumbers. As the higher wavenumbers are being populated, the numerical dissipation rate increases until the decay-rate exponents ranging between $n = 1.40$ (for 32^3 grid) and $n = 1.43$ (for 128^3 grid) are attained. Thus, the FDV-based ILES is able to capture the $t^{*-1.43}$

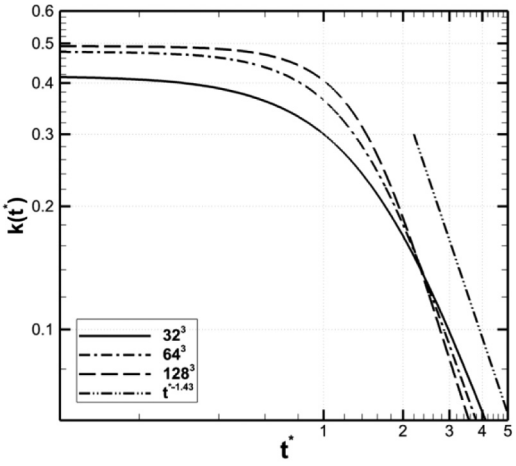

Notes: The $t^{*-1.43}$ decay rate of kinetic energy is also indicated. Profiles are for the implicit LES case with second-order accurate FDV method

Figure 3.
Time history of resolved kinetic energy for different grid resolutions

kinetic-energy decay rate (Kolmogorov, 1941b), especially at the higher grid resolution of 128^3.

Figure 4 shows the time history of enstrophy on the 32^3, 64^3 and 128^3 grids. Enstrophy is computed using $\Omega = \frac{1}{2}\langle \omega \cdot \omega \rangle$, where ω is the vorticity vector and $\langle \cdot \rangle$ denotes spatial averaging. For $t^* > 0.1$, enstrophy increases with time due to vortex stretching that transfers energy to smaller scales with higher velocity gradients. As the turbulent flowfield becomes fully developed, enstrophy peaks around time $t^* = 1.4$. Subsequently, enstrophy undergoes a monotonic decay with time, as numerical damping becomes significant enough to reduce the turbulent kinetic energy. It can be seen that increasing the grid resolution leads to higher enstrophy peaks, indicating a decrease in numerical dissipation with an increase in grid resolution.

Figures 5 and 6 present the time histories of turbulent kinetic energy and enstrophy, respectively, on a 32^3 grid for the linear, quadratic and cubic shape functions. The plots

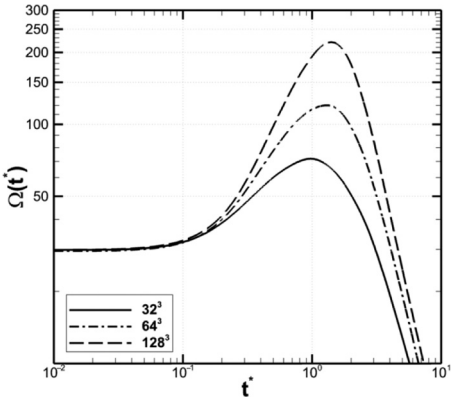

Figure 4.
Time history of enstrophy at different grid resolutions for the implicit LES case

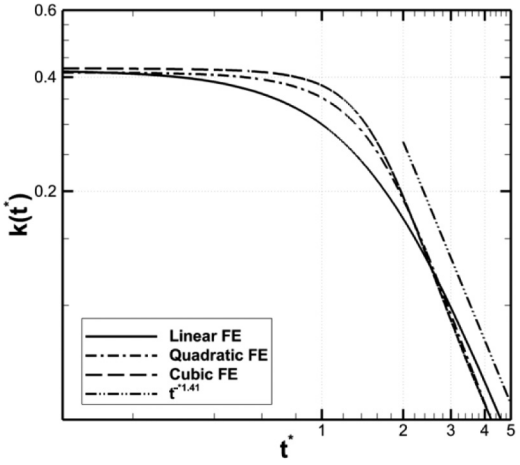

Notes: The $t^{*-1.41}$ decay rate of kinetic energy is also indicated; profiles are for the implicit LES case

Figure 5.
Effects of spatial order-of-accuracy on the temporal decay of resolved kinetic energy on the 32^3 grid

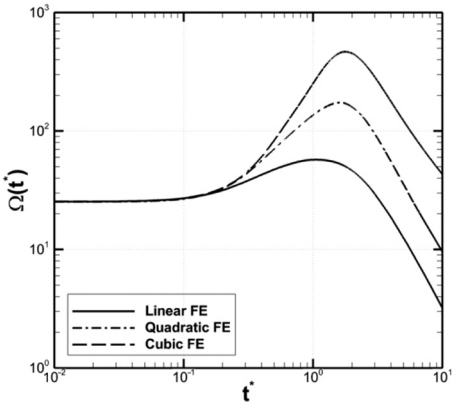

Figure 6.
Effects of spatial order-of-accuracy on the temporal profiles of enstrophy on the 32^3 grid for the implicit LES case

correspond to the FDV/ILES case with no SGS model. Figure 5 shows that the second-order accurate method, with linear finite elements, exhibits the highest kinetic-energy decay rate. This is followed by the third- and fourth-order accurate methods, involving quadratic and cubic finite elements, respectively. The kinetic-energy decay exponents lie between $n = 1.40$ and $n = 1.41$ for all three polynomial orders, which is in good agreement with theoretical range published in Lesieur (2008). However, the best agreement is obtained for the cubic shape functions. The enstrophy profiles in Figure 6 reveal that the higher the order of accuracy, the higher the enstrophy peak. This trend indicates that the fourth-order accurate method is the least dissipative, followed by the third- and second-order accurate methods.

Figure 7 shows a comparison of the temporal evolution of FDV numerical viscosity, calculated from equation (55), for the three grid resolutions. During early computational times ($t^* < 0.9$), the numerical viscosity remains essentially constant, indicating that the

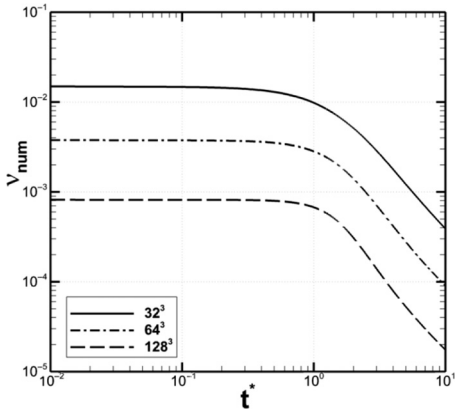

Figure 7.
Effects of grid resolution on the time history of numerical viscosity inherent to ILES/FDV

initial flowfield is dominated by vortices corresponding to low wavenumber modes. This suggests that the turbulent energy cascade has not yet developed so as to cause energy dissipation at high wavenumbers. Once the turbulent flowfield is fully developed and the higher wavenumber modes of the energy spectrum are populated for time $t^* > 1.0$, the magnitude of numerical viscosity decreases monotonically with time due to the dissipation of kinetic energy. In Figure 8, the time history of numerical dissipation rate is shown for the three grids. Initially, the numerical dissipation rate increases with time, but only gradually, until it reaches a peak value around time $t^* \approx 0.9$. Subsequently, the dissipation rate decays monotonically due to the non-linear energy cascade process. Furthermore, Figures 7 and 8 show that as the grid is refined, the magnitudes of both numerical viscosity and dissipation rate decrease, as expected. At the grid resolution of 128^3, the numerical dissipation shows a prominent peak at around $t^* \approx 1.0$, which is the time for which enstrophy is maximized (Figure 4).

5.3 Computations with SGS closures

The discussion in Section 5.2 indicates that the FDV method provides adequate numerical dissipation to maintain stability when performing ILES of isotropic turbulence. In this

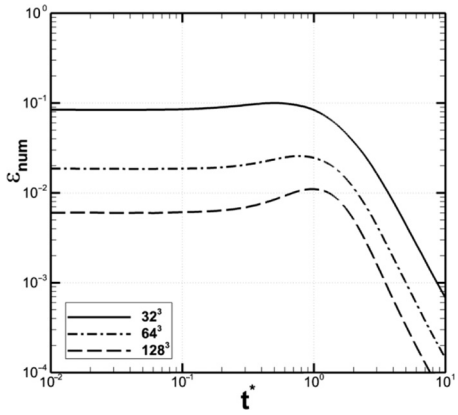

Figure 8.
Effects of grid resolution on the time history of numerical dissipation rate inherent to ILES/FDV

section, we present the results obtained from large-eddy simulations with the standard Smagorinsky and dynamic Smagorinsky SGS models.

Figures 9 and 10 present the time histories of resolved kinetic energy and enstrophy on the 32^3 grid. These figures show that the Smagorinsky model is the most dissipative, as reflected in the lowest magnitudes of both turbulent kinetic energy and enstrophy. In general, the dynamic Smagorinsky model is marginally less dissipative than the other two cases. Figure 11 presents the energy spectra at time $t^* = 10$ for the three LES closures on the 32^3 grid. This figure shows again that the Smagorinsky model is the most dissipative among the three closures, due to the lowest $E(k)$ seen for this model. The dynamic Smagorinsky model tends to better capture the energy spectrum within the inertial subrange through a more accurate estimation of turbulent eddy-viscosity. One also notices that for the 32^3 grid, all three closures are under-dissipative at wavenumbers close to the cut-off wavenumber.

We now present a comparison of the three LES cases on the 64^3 grid. Figures 12 and 13 show the temporal evolution of resolved kinetic energy and enstrophy, respectively, on the 64^3 grid. In Figure 12, all three LES cases show a kinetic-energy decay rate of $t^{*-1.40}$ in the fully developed turbulence regime. It is evident from both kinetic energy and enstrophy plots that in the developed turbulence regime, all three LES closures show

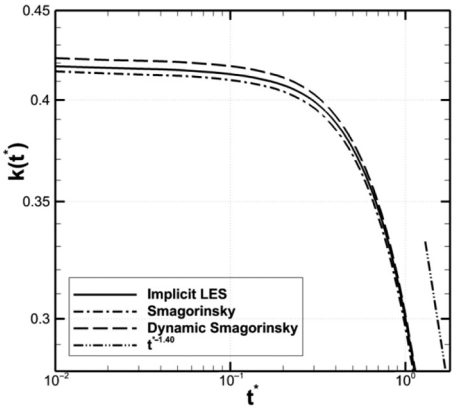

Figure 9.
Comparison of the time histories of resolved kinetic energy for the three LES cases on the 32^3 grid

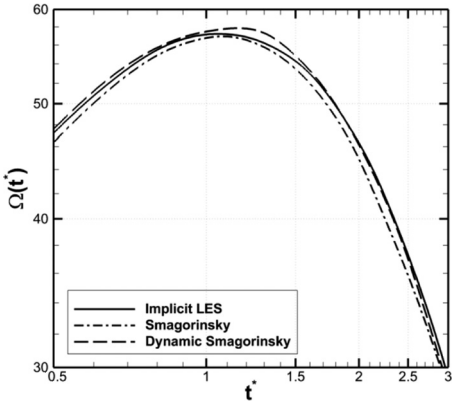

Figure 10.
Comparison of the time histories of enstrophy for the three LES cases on the 32^3 grid

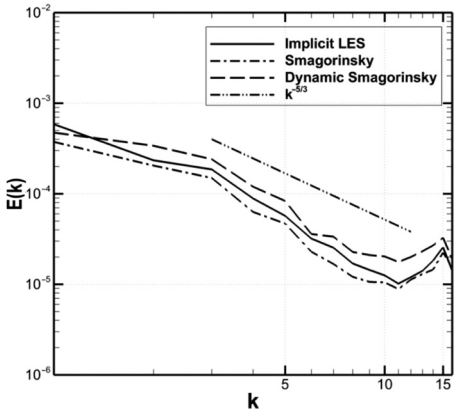

Figure 11.
Comparison of energy spectra for the three LES cases at time $t^* = 10$ on the 32^3 grid

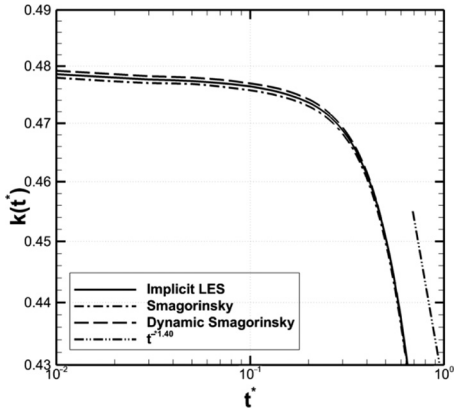

Figure 12.
Comparison of the time histories of resolved kinetic energy for the three LES cases on the 64^3 grid

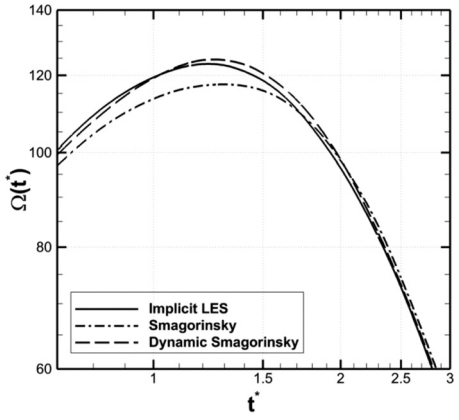

Figure 13.
Comparison of the time histories of enstrophy for the three LES cases on the 64^3 grid

similar dissipative behavior, although the standard Smagorinsky case is marginally more dissipative than the others. In Figure 14, energy spectra at time $t^* = 7$ on the 64^3 grid are shown. When compared to the corresponding spectra for the 32^3 grid, these spectra show improved agreement with the Kolmogorov's $k^{-5/3}$ scaling within the inertial subrange. However, the smallest resolved scales still suffer from low numerical damping.

Figures 15 and 16 present the time histories of turbulent kinetic energy and enstrophy on the 128^3 grid. In the developed turbulence regime, the $t^{*-1.43}$ kinetic-energy decay rate is recovered for the three LES cases, as shown in Figure 15. The plots of enstrophy in Figure 16 are consistent with the previous results, with the standard Smagorinsky model showing slightly greater dissipation than the others. The energy spectra at time $t^* = 5$ on the 128^3 grid are shown in Figure 17. It is evident that the Kolmogorov's $k^{-5/3}$ law in the inertial subrange is better recovered than for the two coarser grids.

Figure 18 compares the temporal profile of numerical viscosity in the FDV-ILES simulation with the temporal profiles of eddy viscosities in the standard Smagorinsky and dynamic Smagorinsky LES simulations. Figure 18(a), 18(b) and 18(c) present these comparisons for the 32^3, 64^3 and 128^3 grids, respectively. For a finite number of flow realizations, we also show the numerical viscosity inherent to the SUPG finite element

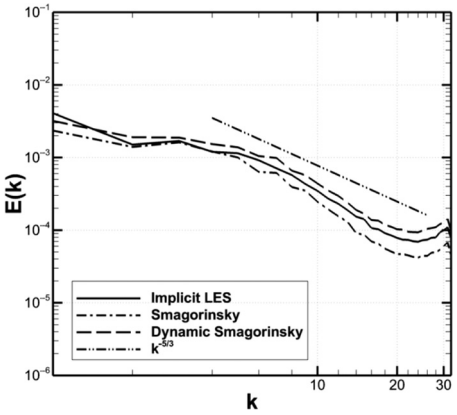

Figure 14.
Comparison of energy spectra for the three LES cases at time $t^* = 7$ on the 64^3 grid

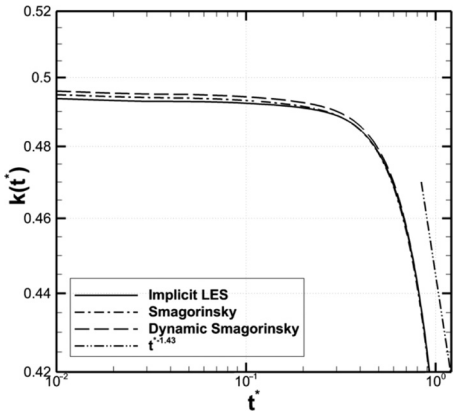

Figure 15.
Comparison of the time histories of resolved kinetic energy for the three LES cases on the 128^3 grid

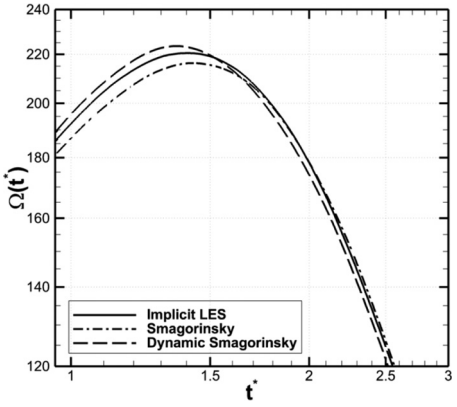

Figure 16.
Comparison of the time histories of enstrophy for the three LES cases on the 128^3 grid

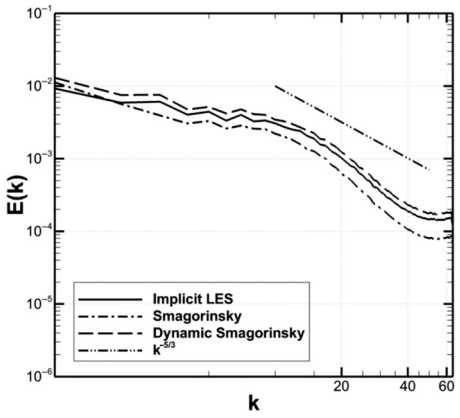

Figure 17.
Comparison of energy spectra for the three LES cases at time $t^* = 5$ on the 128^3 grid

method, calculated from equation (57). It is to be noted that the SUPG numerical viscosity is computed using the FDV-ILES Flowfield at the instances indicated in Figure 18. This approach facilitates a direct comparison of the FDV and SUPG numerical viscosities for a given flowfield.

Figure 18(a) shows that for $t^* < 0.2$, the numerical viscosity for FDV-ILES has a marginally higher magnitude than the eddy viscosities for the two SGS cases. The slightly higher FDV viscosity is not a significant trend, as for $t^* < 0.2$, the turbulence has not yet developed fully. The two SGS viscosities increase marginally during the $0.1 < t^* < 2$ period, but decrease monotonically with time subsequently. Additionally, for $t^* < 0.1$, the ILES, LES and SUPG viscosities remain nearly constant, suggesting that the turbulence has not yet attained a fully developed state characterized by a non-linear energy cascade process. An important observation in Figure 18(a) is that the SUPG numerical viscosity is consistently higher than the other three viscosities. In fact, the SUPG viscosity is nearly an order of magnitude greater than the FDV viscosity at all the flow realizations shown here. Similar trends are observed for 64^3 and 128^3 grids in Figure 18(b) and (c), respectively. It can be seen from Figure 18(a)-(c) that the viscosity magnitudes show an overall decrease with an increase in grid resolution. Further, grid refinement delays the time at which SGS viscosity profiles peak. For the three grids, the FDV-ILES viscosity is the lowest in the fully developed

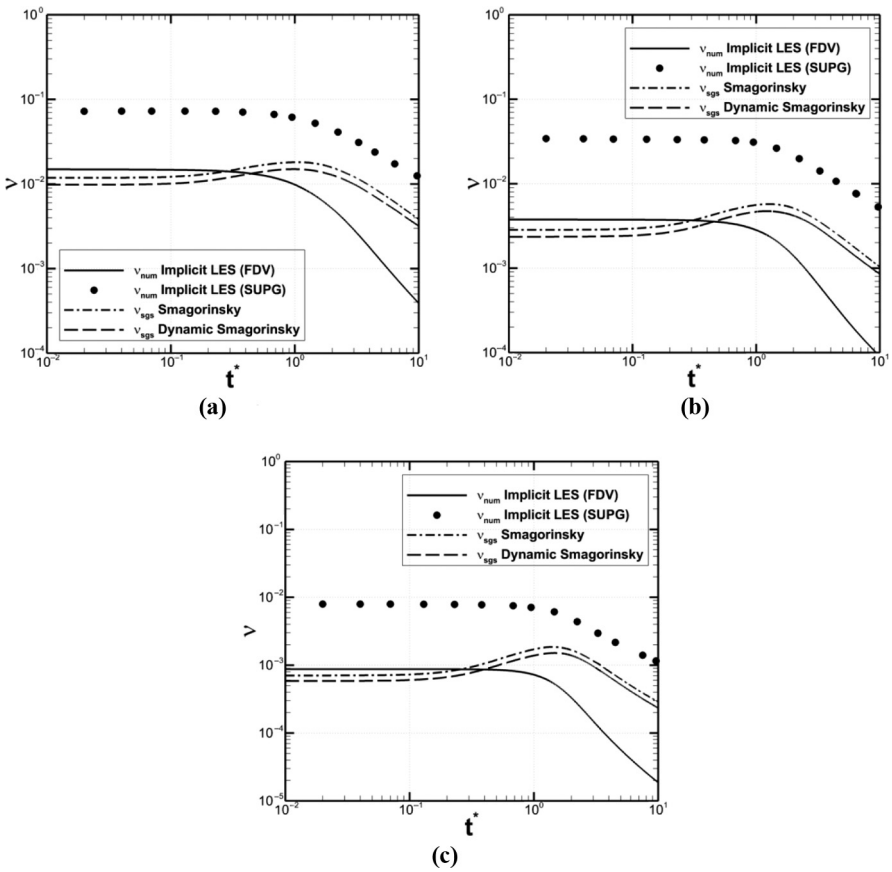

Figure 18. Comparison of temporal profiles of the FDV/ILES numerical viscosity, eddy viscosities of the two SGS/LES cases, and of the numerical viscosity of the SUPG method for: (a) 32^3, (b) 64^3 and (c) 128^3 grids

turbulence regime. The quantitative comparison of the FDV, SGS and SUPG viscosities is the most significant contribution of this study, with potential implications for the field of implicit LES of turbulent flows.

Figure 19 shows a comparison of the time history of dissipation rates in the FDV/ILES and the two SGS/LES simulations. Figure 19(a), 19(b) and 19(c) shows these comparisons on the 32^3, 64^3 and 128^3 grids, respectively. Figure 19(a) shows that during initial times, the dissipation rates for all three cases are essentially constant in time. Subsequently, for $t^* > 0.2$, they undergo a marginal increase in time up to $t^* = 1$. At later computational times, the dissipation rates decay monotonically. The numerical dissipation rate in the FDV/ILES simulation has marginally higher magnitudes during the early stages, but undergoes a steeper decay at later times. Similar trends are observed for the 64^3 and 128^3 grids, except that the magnitudes of dissipation rates decrease as the grid is refined.

The effects of the interactions between the FDV scheme and a SGS model can be assessed by monitoring the effective viscosity, which is defined as the equivalent viscosity representing the energy cascade from the kth wavenumber mode to the modes located beyond the cutoff wavenumber k_c (Ciardi *et al.*, 2005). The effective numerical

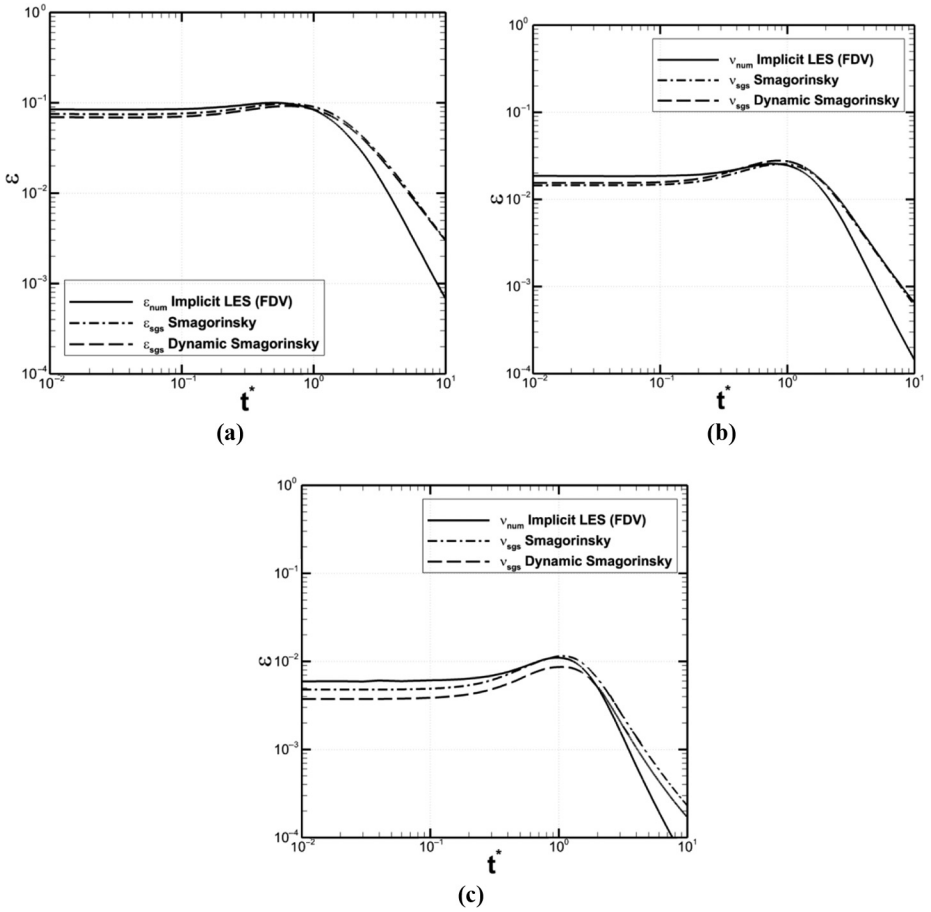

Figure 19.
Comparison of temporal profiles of dissipation rates of the FDV/ILES case, and the two SGS/LES cases for: (a) 32^3, (b) 64^3 and (c) 128^3 grids

viscosity in the FDV/ILES simulation and the effective SGS eddy-viscosity for the two LES cases can be evaluated using the following expressions (Domaradzki *et al.*, 2003; Levasseur *et al.*, 2006):

$$\nu_{\text{eff}}^{\text{num}}(k) = \frac{\varepsilon_{\text{num}}(k)}{2k^2E(k)} \tag{73}$$

$$\nu_{\text{eff}}^{\text{sgs}}(k) = \frac{\varepsilon_{\text{sgs}(k)}}{2k^2E(k)} \tag{74}$$

Figure 20 shows a comparison of the spectra of effective viscosities for FDV/ILES and for the two SGS/LES runs. Figure 20(a), 20(b) and 20(c) shows these spectra for the 32^3, 64^3 and 128^3 grids, respectively, at the dimensionless time $t^* = 3$. Also presented are numerical viscosity spectra of the SUPG method, which are computed for the same flow realization as the FDV-ILES run. The SUPG viscosity spectrum is computed from the following equation:

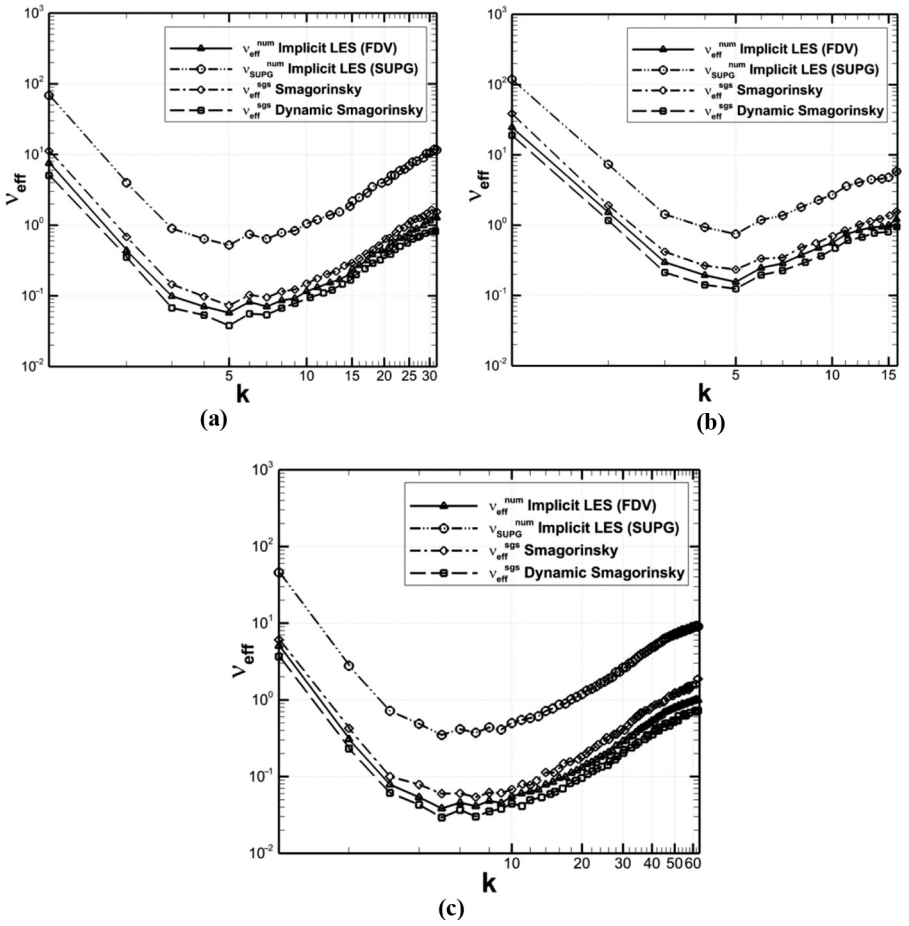

Figure 20.
Comparison of spectra of effective numerical viscosities of the three LES cases, and the numerical viscosity of the SUPG method for: (a) 32^3, (b) 64^3 and (c) 128^3 grids at $t^* = 3$

$$\widehat{v}_{\mathrm{SUPG}}(k) = \sqrt{\sum_{|\boldsymbol{k}'|=k} \widehat{v}_{\mathrm{SUPG}}(\boldsymbol{k}', t)\, \widehat{v}^{*}_{\mathrm{SUPG}}(\boldsymbol{k}', t)} \tag{75}$$

where $\widehat{v}^{*}_{\mathrm{SUPG}}(\boldsymbol{k}',t)$ is the complex conjugate of $\widehat{v}_{\mathrm{SUPG}}(\boldsymbol{k}',t)$.

As can be seen in Figure 20(a), the four viscosity spectra decrease up to wavenumber $k \approx 5$, and then increase with wavenumber reaching a maximum near the cutoff wavenumber. The increase in effective viscosity at higher wavenumbers was also seen in the works of Ciardi *et al.* (2005) and Thornber *et al.* (2007). The decrease in viscosity spectrum at low wavenumbers and the increase at high wavenumbers are desired trends, as the anticipation is for numerical viscosity to be active at high wavenumbers so as to account for the dynamics of scales smaller than the cutoff wavenumber. At all wavenumbers, the numerical viscosity spectrum of the SUPG method is substantially higher than that of FDV/ILES, as well as of the two SGS/LES cases. This behavior is consistent with the higher viscosities seen for SUPG in Figure 18. Similar trends are observed for the 64^3 and 128^3 grids, as shown in Figure 20(b) and (c), respectively.

6. Conclusions

This study investigates the extension of the FDV scheme to large-eddy simulations of decaying isotropic turbulence. Two explicit LES SGS closures, the standard Smagorinsky and the dynamic Smagorinsky models, were implemented and coupled with the FDV scheme. A finite element-based generalized top-hat test filter was used for the dynamic model. The two SGS closures, as well as the implicit LES based on the numerical dissipation inherent to FDV, are investigated and compared for the case of freely decaying incompressible, inviscid isotropic turbulence. The energy spectra from the implicit LES computations show reasonable agreement with the Kolmogorov's $k^{-5/3}$ power-law in the inertial subrange, with the spectra moving closer to the Kolmogorov scaling at higher grid resolutions. The FDV scheme also captures with reasonable accuracy the $t^{*-1.43}$ kinetic-energy decay rate, particularly at the 128^3 grid resolution.

A new formulation for the numerical viscosity inherent to the FDV scheme was developed, and quantified both in physical and spectral spaces. Furthermore, a detailed comparison of the viscosities due to FDV/ILES, SGS/LES and SUPG methods was undertaken. It is seen that the FDV method has the lowest viscosity in the fully developed turbulence regime, while the SUPG/FEM method suffers from the highest viscosity at all times. The results from this study suggest that implicit LES based on the viscosity inherent to FDV scheme shows promise for large-eddy simulations of more complex turbulent flows.

References

Bidadi, S. and Rani, S.L. (2015), "Investigation of numerical viscosities and dissipation rates of second-order TVD-MUSCL schemes for implicit large-eddy simulation", *Journal Computational Physics*, Vol. 281, pp. 1003-1031.

Brooks, A.N. and Hughes, T.J.R. (1982), "Streamline upwind/Petrov-Galerkin formulations for convection dominated flows with particular emphasis on the incompressible Navier-Stokes equations", *Computer Methods in Applied Mechanics and Engineering*, Vol. 32, pp. 199-259.

Canabal, F. and Frendi, A. (2006), "Study of the ignition over-pressure suppression technique by water addition", *Spacecraft and Rockets*, Vol. 43, pp. 853-865.

Chalot, F., Marquez, B., Ravachol, M., Ducros, F., Nicoud, F. and Poinsot, T. (1998), "A consistent finite approach to large-eddy simulation", Paper Presented at 29th AIAA Fluid Dynamic Conference, pp. 98-2652.

Chung, T.J. (2002), *Computational Fluid Dynamics*, Cambridge University Press, New York, NY.

Ciardi, M., Sagaut, P., Klein, M. and Dawes, W.N. (2005), "A dynamic finite volume scheme for large-eddy simulation on unstructured grids", *Journal of Computational Physics*, Vol. 210 No. 2, pp. 632-655.

Domaradzki, J.A., Xiao, Z. and Smolarkiewicz, P.K. (2003), "Effective eddy viscosities in implicit large eddy simulations of turbulent flows", *Physics of Fluids*, Vol. 15 No. 12, pp. 3890-3893.

Erlebacher, G., Hussaini, M.Y., Speziale, C.G. and Zang, T.A. (1992), "Toward the large-eddy simulation of compressible turbulent flows", *Journal of Fluid Mechanics*, Vol. 288, pp. 155-185.

Garnier, E., Adams, N. and Sagaut, P. (2009), *Large Eddy Simulation for Compressible Flows*, Springer.

Garnier, E., Mossi, M., Sagaut, P., Comte, P. and Deville, M. (1999), "On the use of shock-capturing schemes for large-eddy simulation", *Journal of Computational Physics*, Vol. 153 No. 2, pp. 273-311.

Germano, M., Piomelli, U., Moin, P. and Cabot, W.H. (1991), "A dynamic subgrid-scale eddy viscosity model", *Physics of Fluids A*, Vol. 3 No. 7, pp. 1760-1765.

Girgis, B., Rani, S.L. and Frendi, A. (2015), "Flowfield dependent variation method: A numerical scheme for the solution of low- to high Mach number flow problems", *International Journal of Numerical Methods for Heat & Fluid Flow*, Vol. 26 No. 5, pp. 1486-1525.

Jansen, K.E. (1999), "A stabilized finite element method for computing turbulence", *Computer Methods in Applied Mechanics and Engineering*, Vol. 174, pp. 299-317.

Jansen, K.E. (1995), "Preliminary large-eddy simulation of flow around a NACA 4412 airfoil using unstructured grids", CTR Annual Research Briefs, Center for Turbulence Research, NASA Ames/Stanford University, Stanford, CA, pp. 61-72.

Kolmogorov, A.N. (1941a), "The local structure of turbulence in an incompressible fluid at very high Reynolds numbers", *Soviet Physics Uspekhi*, Vol. 30, pp. 301-305.

Kolmogorov, A.N. (1941b), "On degeneration of isotropic turbulence in an incompressible viscous liquid", *Doklady Akademii Nauk SSSR*, Vol. 31, pp. 538-541.

Lesieur, M. (2008), *Turbulence in Fluids*, 4th ed., Springer, Dordrecht.

Levasseur, V., Sagaut, P., Chalot, F. and Davroux, A. (2006), "An entrophy-variable-based VMS/GLS method for the simulation of compressible flows on unstructured grids", *Computer Methods in Applied Mechanics and Engineering*, Vol. 195, pp. 1154-1179.

Lilly, D.K. (1992), "A proposed modification of the Germano subgrid-scale closure method", *Physics of Fluids A*, Vol. 4 No. 3, pp. 633-635.

Martín, M.P., Piomelli, U. and Candler, G.V. (2000), "Subgrid-scale models for compressible large-eddy simulations", *Theoretical and Computational Fluid Dynamics*, Vol. 13 No. 5, pp. 361-376.

Moin, P., Squires, K., Cabot, W. and Lee, S. (1991), "A dynamic subgrid model for compressible turbulence and scalar transport", *Physics of Fluids A*, Vol. 3 No. 11, pp. 2746-2757.

Moon, S.Y., Sohn, C.H. and Lee, C.W. (2001), "Applications of a flowfield-dependent mixed explicit-implicit (FDMEI) method to heat and fluid dynamics problems", *Numerical Heat Transfer*, Vol. 39, pp. 389-404.

Oberlack, A. (2002), "On the decay exponent of isotropic turbulence", *Proceedings in Applied Mathematics and Mechanics*, Vol. 1 No. 1, pp. 294-297.

Pope, S.B. (2000), *Turbulent Flows*, Cambridge University Press, Cambridge.

Richardson, G.A., Cassibry, T.J., Chung, T.J. and Wu, S.T. (2010), "Finite element form of FDV for widely varying flowfield", *Journal of Computational Physics*, Vol. 229 No. 1, pp. 145-167.

Richardson, G.A. and Chung, T.J. (2002), "Computational relativistic astrophysics using the flowfield-dependent variation theory", *The Astrophysical Journal Supplement Series*, Vol. 139 No. 2, pp. 539-563.

Samtaney, R., Pullin, D.I. and Kosovic´, B. (2001), "Direct numerical simulation of decaying compressible turbulence and shocklet statistics", *Physics of Fluids*, Vol. 13 No. 5, pp. 1415-1430.

Smagorinsky, J.S. (1963), "General circulation experiments with the primitive equations (I). The basic experiment", *Monthly Weather Review*, Vol. 91 No. 3, pp. 99-164.

Tejada-Martínez, A.E. and Jansen, K.E. (2003), "Spatial test filters for dynamic model large-eddy simulation on finite elements", *Communications in Numerical Methods in Engineering*, Vol. 19 No. 3, pp. 205-213.

Tejada-Martínez, A.E. and Jansen, K.E. (2004), "A dynamic Smagorinsky model with dynamic determination of the filter width ratio", *Physics of Fluids*, Vol. 16 No. 7, pp. 2514-2528.

Thornber, B., Mosedale, A. and Drikakis, D. (2007), "On the implicit large eddy simulations of homogeneous decaying turbulence", *Journal Computational Physics*, Vol. 226 No. 2, pp. 1902-1929.

Vreman, B., Guerts, B. and Kuerten, H. (1995), "A priori tests of large-eddy simulation of the compressible plane mixing layer", *Journal of Engineering Mathematics*, Vol. 29 No. 4, pp. 299-327.

Vreman, B., Guerts, B. and Kuerten, H. (1997), "Large-eddy simulation of turbulent mixing layers", *Journal of Fluid Mechanics*, Vol. 339, pp. 357-390.

Yakhot, V. (2004), "Decay of three-dimensional turbulence at high Reynolds numbers", *Journal of Fluid Mechanics*, Vol. 505, pp. 87-91.

Yoon, K.T. and Chung, T.J. (1996), "Three dimensional mixed explicit-implicit generalized Galerkin spectral element methods for high speed turbulent compressible flows", *Computer Methods in Applied Mechanics and Engineering*, Vol. 135 Nos 3/4, pp. 343-367.

Yoon, K.T., Moon, S.Y., Garcia, S.A., Heard, G.W. and Chung, T.J. (1998), "Flowfield-dependent mixed explicit-implicit (FDMEI) methods for high and low speed and compressible and incompressible flows", *Computer Methods in Applied Mechanics and Engineering*, Vol. 151 Nos 1/2, pp. 75-104.

Further reading

Lilly, D.K. (1966), "On the application of the eddy viscosity concept in the inertial subrange of turbulence", *NCAR Manuscript*, Boulder, CO.

Corresponding author

Abdelkader Frendi can be contacted at: kader.frendi@uah.edu